Journal of Breath Research

PAPER

3D computational fluid and particle dynamics simulations: metrics of aerosol capture by impaction filters*

IOP Publishing J. Breath Res. 18 (2024) 016002 https://doi.org/10.1088/1752-7163/acfe32

Journal of Breath Research

RECEIVED
19 March 2023

REVISED
24 August 2023

ACCEPTED FOR PUBLICATION
28 September 2023

PUBLISHED
10 October 2023

PAPER

3D computational fluid and particle dynamics simulations: metrics of aerosol capture by impaction filters*

Veruska Malavé, Kavita Jeerage, Edward Garboczi and Tara Lovestead**

Applied Chemicals and Materials Division, National Institute of Standards and Technology. Boulder, CO 80305, United States of America
**Author to whom any correspondence should be addressed.

E-mail: veruska.malave@nist.gov

Keywords: computational fluid and particle dynamics (CFPD), aerosol analysis, particle deposition, impaction filter, clinical breath analysis, exposure and forensic science

Abstract

Human studies provide valuable information on components or analytes recovered from exhaled breath, but there are limitations due to inter-individual and intra-individual variation. Future development and implementation of breath tests based on aerosol analysis require a clear understanding of how human factors interact with device geometry to influence particle transport and deposition. The computational fluid and particle dynamics (CFPD) algorithm combines (i) the Eulerian approach to fluid dynamics and (ii) the Lagrangian approach to single particle transport and deposition to predict how particles are carried in fluids and deposited on surfaces. In this work, we developed a 3D multiscale CFPD model to provide insight into human factors that could be important to control or measure during sampling. We designed the model to characterize the local transport, spatial distribution, and deposition of polydisperse particles in a single impaction filter of a commercial aerosol collection device. We highlight the use of decoupling numerical strategies to simultaneously quantify the influence of filter geometry, fluid flowrate, and particle size. Our numerical models showed the remarkable effect of flowrate on aerosol dynamics. Specifically, aerosol mass deposition, spatial distribution, and deposition mechanisms inside the filter. This work as well as future studies on the effect of filter geometry and human factors on aerosol collection will guide the development, standardization, and validation of breath sampling protocols for current and emerging breath tests for forensic and clinical applications.

1. Breath research

While exhaled breath primarily consists of gases and volatile organic compounds, breath also contains aerosol particles that can remain suspended in air for hours. Since the onset of the COVID-19 pandemic, there is an urgent need to better understand aerosols and their role in the spread of respiratory viruses [1]. Aerosol particles originate from the airway lining fluid [2] composed of surfactants that form the blood-air interface. Particles form during inhalation due to the reopening of small airways (closed during the previous exhalation), which destabilizes airway surfaces. Empirical evidence for this mechanism includes the increase in exhaled particles with ventilation ratio. Specifically, increasing the ventilation ratio from approximately 0.2 (normal tidal breathing) to 0.8 results in an exponential increase in the particle concentration [3, 4]. A separate study, in which breath flowrates and the exhalation volume were controlled, demonstrated that exhalation to residual volume, which allows small airways to close, also increased exhaled particle concentration [5]. Implementing low-lung-volume breath holds has also been shown to increase exhaled particle concentrations [6]. Lung surfactant is a mixture of approximately 90% lipids and 10% proteins that lower the surface tension within the alveoli [7]; therefore, aerosol particles have been analyzed for protein [8, 9] and phospholipid content [2, 10, 11]. Phospholipids

* Contribution of NIST; not subject to U.S. copyright. Certain commercial equipment, instruments, software, or materials are identified in this paper in order to specify the experimental procedure and virtual experimentation adequately. Such identification is not intended to imply recommendation or endorsement by NIST, nor is it intended to suggest that the materials or equipment identified are necessarily the best available for the purpose.

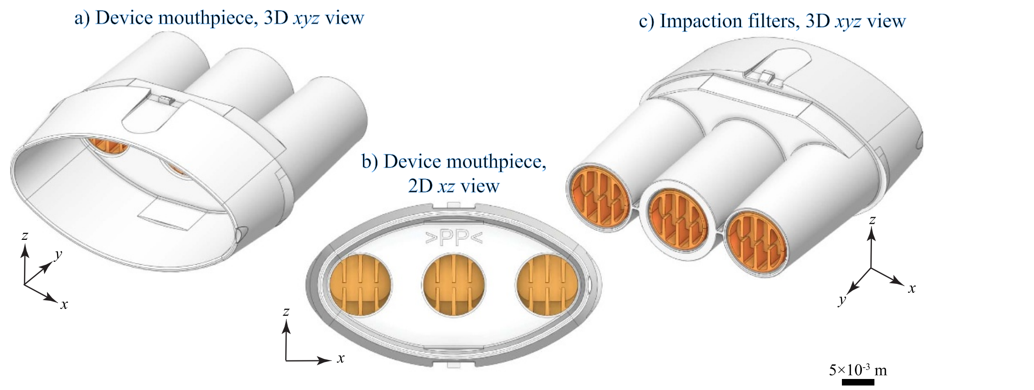

Figure 1. Commercial aerosol collection device consisting of a shell structure (depicted in off-white) with a mouthpiece shown in 3D (a) and 2D (b) views, and three impaction filters (depicted in orange) shown in 3D (c). *The outer housing and removable caps are not pictured.*

have been quantified in aerosol particles collected by electret filtration [10] or by inertial impaction [2, 11], providing intriguing evidence that the mass of phospholipid is proportional to the total mass of exhaled particles and thus, has potential to be used for normalization. Studies conducted within the last two decades using optical particle counters sensitive to submicrometer particles have concluded that 80%–90% of exhaled aerosols are smaller than 1 μm [12] and that no particles are larger than 4 μm [13]. The absence of large particles is due to gravitational settling or sedimentation during transport through the respiratory system and exhalation [3].

Aerosol particle analysis has potential for public health and safety or occupational exposure screening. Aerosols, or their residues, have been recovered from disposable paper surgical masks and from plastic respirator surfaces and face shields [14], for applications such as cancer screening [15]. Aerosol particle analysis also has the potential to detect systemic drugs. For example, the metabolites normorphine and dihydromorphone were recovered from exhaled breath condensate (EBC) collected from patients infused with the opioids morphine and hydromorphone, respectively [16]. Δ9 tetrahydrocannabinol (Δ9 THC), a drug molecule with very low volatility [17], has primarily been recovered from filtration devices that focus on the aerosol fraction of breath. For example, electrostatic filters have been used in a variety of settings to collect aerosol samples to detect analytes indicative of drug use from patients entering drug-treatment clinics [18], and individuals suspected of impaired driving [19], more recently, medical cannabis patients [20] and recreational cannabis users [21, 22]. Due to the advantages of simultaneously capturing multiple samples, a simple device employing impaction filters, BreathExplor by Munkplast AB, was developed and first described in 2018 [23]. Although the number of published studies with this device remains small, findings have demonstrated recovery of (a) two phospholipids found in lung surfactant [23], (b) methadone from individuals undergoing treatment [23], (c) drugs of abuse in a field study of more than 1200 individuals attending a music festival [24], and (d) Δ9 THC 1 h after cannabis use [25].

Figure 1 shows a CAD schematic of this device, which is made of injection-molded medical grade polypropylene; a mouthpiece that the user exhales to (figures 1(a) and (b)), and three separate and parallel impaction filters designed to capture aerosol particles as the breath passes through (figures 1(b) and (c)). While the general principle for aerosol particle capture by the BreathExplor device is understood to be impaction driven by the eight alternating baffles within each filter, we lack a comprehensive understanding of the details of aerosol particle transport, distribution, and deposition through the filter. Human studies provide valuable information on recovered components or analytes, but there are limitations due to inter-individual and intra-individual variation. As we will show, computational simulations can deepen our understanding of some fundamental aspects of breath sampling with impaction filter devices.

2. Computational fluid and particle dynamics (CFPD)

Computational fluid dynamics (CFD) has significantly contributed to exhaled breath research. For instance, CFD has been used to design breath devices for lung cancer diagnosis [26], to optimize chamber geometries in devices for detecting chronic kidney disease via chemical sensors [27], and to study the generation of submicrometer particles in exhaled breath [28]. However, CFD methods alone do not solve actual individual dispersion or trajectories of particles. In contrast, CFPD methods can be used to investigate local dynamics and trace the trajectory of polydisperse aerosols of different shapes (with any shape factor) and sizes in the ultrafine scale ($\leqslant 0.2\,\mu$m) and larger. This numerical approach has provided complete-airway deposition modeling of the human respiratory system by solving spatially and temporally complex fluid-particulate dynamics formulations [29–31]. CFPD has become a key component for understanding the next-generation of respiratory drug delivery [32–36]; diagnosing obstructive lung diseases [37]; studying exhaled particles during respiratory events [38] and airborne transmission of infectious disease [39–43], including COVID-19 [44–47] and other forms of bioaerosol transmission [48, 49], conducting risk assessment for toxic air pollutants [50, 51], and collecting exhaled aerosols and saliva microdroplets within EBC devices with different geometries [52, 53].

CFPD methods can be used to support the design and implementation of breath sampling devices by simulating and predicting the transport, spatial distribution, and deposition of exhaled particles in any defined 3D structure. Yet, very limited numerical studies are found in the archival literature, particularly ones in which CFPD simulates particle deposition within a breath collection device [52, 53]. We developed a high-fidelity 3D multiscale CFPD parametric model of a single impaction filter of the BreathExplor device to understand the contribution of filter geometry, fluid flowrate, and aerosol particle size to particle deposition. By coupling multiscale dynamics of small polydisperse aerosol particles diluted in a fluid stream inside complex spaces, we provide a guide tool for standardizing metrics that will promote pathways to investigate the influence of human factors for any impaction filter device and improve reproducibility for biomarker discovery and quantitation of compounds important for clinical and forensic applications.

3. Methodology

3.1. Model geometry and discretization

This work focused on the analysis of fluid flow and particle dynamics in one of the three filters of a commercially available breath aerosol collection device (BreathExplor). Simulating the entire device (figure 1) would require accounting for breath flow changes in the mouthpiece and how the flow would be distributed into the three separate filters at the mouthpiece exit. The purpose of this study is to show the power of CFPD to aid in understanding human factors, not to optimize or validate filter geometry, thus the simplification is justified. The filter shown in figures 1(b) and (c) comprises two conforming and separable pieces. Figure 2 shows the process of generating the 3D computational domain and mesh. This filter has eight 0.6 mm thick baffles arranged in a sequential order from inlet to outlet with four alternating baffles per half-piece filter, as shown in figure 2(a). The exhaled breath moves downstream, i.e. from the inlet to the outlet of the filter in the positive y direction, through the enclosed 1.08×10^{-6} m^3 fluid domain shown in figure 2(b). This filter has a complex geometry due to the baffle's spline design and a nearly cylindrical geometry with an approximate radius R of 4.8 mm and a length L of 22 mm.

The 3D computational domain in figure 2(b) was discretized by the definition of a mesh formed by polyhedral cells, as depicted in figures 2(c)–(f), for accurate gradient approximations. Cells made up of polyhedra have been proven to be more computationally efficient and with comparable accuracy for modeling particle transport with respect to other types of discretization elements [54]. The two primary quality metrics of a mesh are (1) cell skewness, which is the measure of deviation from the ideal shape being 0–0.25 (excellent) and 0.98–1 (unacceptable); and (2) orthogonal quality, which describes how much the mesh criteria are within the correct range that is valid for physical value prediction, being 0–0.001 (poor) to 0.95–1 (excellent). In our model, high-quality cell metrics of average skewness of 0.019 and average orthogonal quality of 0.88 were achieved.

Model discretization was created in Ansys Fluent Meshing 2022 R2 software (Canonsburg, Pennsylvania) and mesh independence was established based on the fluid dynamics of 0.8-L $\cdot$ s^{-1} saturated air flowing from the inlet to the outlet of the filter. The mesh of this model was chosen by comparing the volume-average of velocity magnitude as well as the overall pressure drop between three meshes of approximately 0.88 average orthogonal quality for quality consistency purposes. These meshes had higher degrees of spatial resolution consisting of (a) 285 150 cells, (b) 564 796 cells, and (c) 1437 135 cells with normalized grid spacing ratios of 5.89, 2.81, and 1.00, respectively. Both meshes in (a) and (b) showed relatively close fluid velocity magnitude versus the mesh in (c) with an error of 0.84%, but differ in pressure drop by 10.91% (285 150-cell mesh) and 0.72% (564 796-cell mesh), respectively, when compared to the 1437 135-cell mesh. Hence, for computational cost effectiveness, our final computational mesh consisted of 564 796 cells, which had 1849 670 nodes and a maximum characteristic cell length of approximately 1.74×10^{-4} m. To aid capturing flow gradients and particle motions near the wall, characteristic cell lengths of up to approximately 3.82×10^{-8} m were set in the boundary layers by smooth-transition meshing, see figures 2(e) and (f). A histogram of the cell quality metrics of this model in terms of orthogonal quality is shown in figures 2(g).

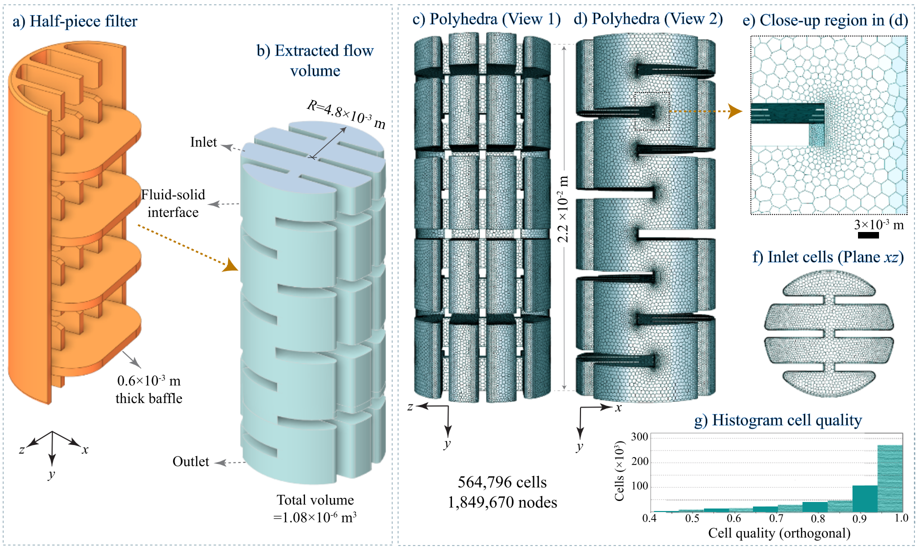

Figure 2. Fluid volume extraction and mesh generation for the computational model: (a) half-piece of impaction filter; (b) fluid domain confined in two-piece filter; view of polyhedral 3D mesh in yz (c) and xy (d); (e) enclosed square region in (d); (f) computational mesh of filter inlet (cross section in $\overline{xz}$); and (g) metrics of cell orthogonal quality.

3.2. Fluid-particulate coupled dynamics: governing laws

Breath flow through the filter was simulated as two distinct phases: (a) the continuous steady-state phase, which is the fluid flow of saturated air as an ideal gas mixture, to study the fluid velocity and viscous profiles at various flowrates; and (b) the discrete unsteady phase to trace the polydisperse small aerosols carried by the fluid flow. Both the fluid flow and the aerosol cloud were injected at the filter inlet (figure 2(b)) and the aerosols were treated as liquid water particles. This formulation solved the continuous phase on an Eulerian fixed mesh while aerosol particles were treated discretely using the Lagrange formulation to calculate the trajectory and fate of each particle separately and interpret deposition mechanisms. Forces that govern the motion of individual particles were simplified by assuming: (i) spherical particles with constant diameter; (ii) only particle translational motion (i.e. non-rotational aerosols); (iii) particle material undergoing neither heat nor mass transfer; and (iv) dilute particulate matter (i.e. the mass and volume fraction of the aerosol cloud was much less than 1%) for a one-way coupling approach. Although the density of liquid water is much larger than that of saturated air, aerosols are expected to be $\approx$1 μm in diameter or smaller but mostly in the submicrometer scale; therefore, gravitational sedimentation was neglected.

3.2.1. *Continuous phase: the fluid flow dynamics*

Because exhaled human breath carries a signature of the morphology of primarily the upstream flow region (i.e. the extrathoracic airways) that highly induces eddies, the fluid flow was considered turbulent. Turbulence in breath has been established even in cases of low Reynolds flows [33, 36, 55] with turbulence intensities of 41% $\pm$ 5% during normal exhalation [55]. Transition to fully turbulent flow conditions can be described by viscous models where the instantaneous stream velocity vector $\mathbf{u}$ of the fluid can be decomposed into the time-averaged velocity $\hat{\mathbf{u}}$ and the turbulence velocity fluctuation. Assuming neither condensation nor gravitational effects, the conservation continuity and momentum relations based on the 3D Reynolds averaged Navier Stokes of the steady-state fluid are presented in equations (1) and (2), respectively:

$$\nabla \cdot \hat{\mathbf{u}} = 0, \tag{1}$$

$$\hat{\mathbf{u}} \cdot \nabla \hat{\mathbf{u}} = -\frac{1}{\rho} \nabla p + (\nu + \nu_T)\, \nabla^2 \hat{\mathbf{u}}, \tag{2}$$

where ρ, ν, and ν_T are the density, kinematic viscosity, and turbulent kinematic viscosity of the gas flow, respectively; and p is the static pressure. The species mass transport relation of the gaseous and vapor species in the fluid used for the numerical solution can be found in [56].

3.2.2. *Discrete phase: aerosol particle transport, distribution, and deposition*

The location and velocity of each particle were traced through the Eulerian mesh by integrating Newton's second law of motion. Instantaneous particle deposition under the effects of accelerating and decelerating fluid flow on particle trajectory was considered to be unsteady (i.e. non-equilibrium particle velocity). As the fluid dynamics of the flow was unaltered by the aerosol cloud, the interphase momentum exchange is primarily governed by $\mathbf{u}$, ρ, and the fluid dynamic viscosity of fluid μ, as well as the diameter and translational velocity of the aerosols, D_a and $\mathbf{u}_a$, respectively. The particle trajectory, aerosol position $\mathbf{x}_a$ and $\mathbf{u}_a$, were solved by integrating the force balance equating the particle inertia with the forces acting on the particle using equations (3) and (4):

$$\frac{d\mathbf{x}_a}{dt} = \mathbf{u}_a, \tag{3}$$

$$m_a \frac{d}{dt}(\mathbf{u}_a) = \mathbf{F}^d + \mathbf{F}^B, \tag{4}$$

where m_a is the aerosol mass, t is time, $\mathbf{F}^d$ is the drag force and $\mathbf{F}^B$ is the contribution of the Brownian-induced force. Brownian diffusion, which is induced by random molecular impact of the flow on submicrometer-size particles, was also implemented as the aerosol cloud had particles in that length scale. $\mathbf{F}^d$ is defined as:

$$\mathbf{F}^d = \frac{3}{4} C_d (\mathbf{u} - \mathbf{u}_a) \mu \frac{m_a}{\rho_a D_a^2} \mathrm{Re}_a, \tag{5}$$

where ρ_a is the density of the aerosol and C_d is the drag coefficient, which depends on the relative Reynolds number with respect to aerosol particles, Re_a, defined as:

$$\mathrm{Re}_a = \frac{\rho D_a |\mathbf{u} - \mathbf{u}_a|}{\mu}. \tag{6}$$

The values of C_d were chosen according to a modified Stokes law that uses a three-term Stokes correlation proposed by the Morsi–Alexander model (1972) [57] for smooth spherical particles and is given by:

$$C_d = a_1 + \frac{a_2}{\mathrm{Re}_a} + \frac{a_3}{\mathrm{Re}_a^2}, \tag{7}$$

where a_1, a_2, and a_3 are constants for a wide range of global Reynolds (Re) numbers, and $\mathrm{Re} = \rho \mathbf{u}/\mu$ ranges from $0 < \mathrm{Re} < 5 \times 10^4$ [57].

To account for aerosol turbulent dispersion, the stochastic discrete random walk model [56, 58] was used so that the turbulent velocity component in $\mathbf{u}$ on the particle trajectories could be implemented. Another metric that has been commonly used to identify the condition of particle transport in fluids is the dimensionless Stokes number St_a, which is the ratio of two timescales: that of the fluid and that of the aerosol cloud. The Stokes number of a single particle in equation (8) characterizes the ability of particles to follow the fluid streamlines by relating the aerosol response time τ_a to changes in flow velocity based on some time characteristic of the flow field τ:

$$\mathrm{St}_a = \frac{\tau_a}{\tau}, \tag{8}$$

where $\tau_a = \frac{\rho_a {D_a}^2}{18\mu}$ and $\tau = \frac{2R}{u}$. According to classical Stokes theory, cases wherein $\mathrm{St}_a <<1$ have been related to particles adjusting very quickly to changes in the flow, dynamic equilibrium is achieved, and particles follow the fluid streamlines (particle advection) [59]. In contrast, particles with a large Stokes number, $\mathrm{St}_a >>1$, are dominated by their inertia, continue along their initial trajectory [59], deviating from the fluid streamlines.

4. Numerical solution

The E–L system of saturated air and aerosol cloud was simulated at $T = 35\,^\circ\mathrm{C}$ and atmospheric pressure, 0.101 MPa, using ANSYS FLUENT 2022 R2 software. Turbulence in exhaled breath was prescribed based on the realizable k-ε viscous model [60] to account for eddies formed in the larynx and oral cavity and set with a 5% turbulent intensity. The implementation of the realizable k-ε viscous model in human breath aerosol deposition in the extrathoracic airways has been validated by *in-situ* and *in-vitro* experiments [61]. A uniform fluid flow profile was assumed and directly injected at the filter inlet, with a flow direction perpendicular to the inlet (i.e. along the y axis). Exhalation flowrates can be expected to vary widely if human subjects are not guided; for example, from $0.01\,\mathrm{L\cdot s^{-1}}$ to $1.2\,\mathrm{L\cdot s^{-1}}$ [62]. Specified exhalation flowrates in particle emission studies include: $0.2\,\mathrm{L\cdot s^{-1}}$–$0.25\,\mathrm{L\cdot s^{-1}}$ [5, 6], $0.4\,\mathrm{L\cdot s^{-1}}$–0.5 = $\mathrm{L\cdot s^{-1}}$ [4], $0.8\,\mathrm{L\cdot s^{-1}}$ [11], and $1.25\,\mathrm{L\cdot s^{-1}}$ [3]. To select (i) a lower limit, we considered the prescribed exhalation flowrate employed in the nitric oxide breath test, which is $0.05\,\mathrm{L\cdot s^{-1}}$ [63]; and to select (ii) an upper limit, we considered the forced expiratory volume exhaled in 1 s, which varies by age, sex, height, and ethnicity [64]. While these values range from 2 L to nearly 6 L, we selected $2.4\,\mathrm{L\,s^{-1}}$ and $3.6\,\mathrm{L\,s^{-1}}$ as plausible upper limits for females and males, respectively.

Considering (i) and (ii) and because the device contains three filters in parallel, we chose a constant flow of one third of the exhalation flowrate, specifically: $0.02\,\mathrm{L\cdot s^{-1}}$, $0.2\,\mathrm{L\cdot s^{-1}}$, $0.4\,\mathrm{L\cdot s^{-1}}$, $0.8\,\mathrm{L\cdot s^{-1}}$, and $1.2\,\mathrm{L\cdot s^{-1}}$. However, further numerical validation of the entire device presented in figure 1 will be needed to confirm the relationship between exhalation flowrate and the flow through each filter. Atmospheric pressure was prescribed at the filter outlet (i.e. zero constant gauge pressure) with no backflow. The species transportation in the fluid flow was set at concentrations that approximately correspond to the end-tidal breath via the weighted-mixing-law of mass fractions: 14.30% oxygen, 4.81% carbon dioxide, 75.96% nitrogen, and 4.76% water vapor. In all flowrate cases, the cell Reynolds number, which is the ratio of the fluid inertial forces to viscous forces across a given cell in the mesh domain, was consistently high in the local flow direction (i.e. moving towards the filter outlet) and low in opposite areas

Table 1. Properties of species considered in simulated breath at 35°C and 0.101 MPa.

Species and particles	Density ($kg \cdot m^{-3}$)	Dynamic viscosity ($mPa \cdot s$)
Oxygen, gas	1.299	1.919×10^{-2}
Nitrogen, gas	1.138	1.663×10^{-2}
Carbon dioxide, gas	1.7878	1.37×10^{-2}
Water, vapor	0.5542	1.34×10^{-2}
Water aerosol, liquid	998.2	1.003

such as underneath the baffles. This suggested the model integration reached numerical stability.

Table 1 reports the thermophysical material properties of the gas, vapor species, and aerosols. Under no-slip shear flow conditions (the relative velocity between the wall and the fluid flow was set to zero), the particle deposition boundary condition considered a particle deposited or 'captured' (its trajectory terminated) upon the first particle-wall collision or contact. The deposition metric was based on the mass fraction of aerosol captured on the filter wall as% *by mass* (i.e. collection based on particle number was not registered). This allowed several different aerosol fate scenarios, singly or in combination, to be present in the numerical model, depending on the dynamics between particle size and fluid flow:

1. *Impaction*: due to inertial forces when there is a sudden change in the direction and magnitude of the flow causing particles to deviate from flow streamlines and remain in their original pathline.
2. *Direct interception*: due to drag forces of the flow that carry aerosols in the fluid streamlines and come close enough to the filter wall. The particle-wall contact is established when an edge of the particle is within particle radius away from the wall, even in cases wherein the aerosol trajectory does not deviate from the fluid streamline [65].
3. *Turbulent dispersion*: due to eddy forces that occur upon abrupt fluid fluctuations, causing particles to continuously undergo motion changes due to their own non-equilibrium (unsteady) state.
4. *Brownian diffusion*: due to random motion of particles when interacting and colliding with fluid molecules.
5. *Loss*: no particle-wall interaction was recorded; particles that remained in the free stream inside the filter were not considered to affect deposition because their mass was negligible.

Particle concentration or number density during breathing has been examined with optical particle counters based on light scattering [5, 6, 62], aerodynamic particle sizers based on time-of-flight measurements [66], a condensation nuclei counter [3, 4], and a scanning mobility particle sizer [62]. When participants exhaled to residual volume (i.e. fully emptied their lungs) and exhaled at $0.1\,L \cdot s^{-1}$–$1.2\,L \cdot s^{-1}$ [5, 62], mean concentrations in particles per liter were: $8500 \times L^{-1}$ [5] and $5300 \times L^{-1}$ [62]. We selected $5000 \times L^{-1}$, but because this system is dilute, being on the order of 10^{-4}% *by mass* of the fluid confined in the filter, the numerical results are representative for other particle number density scenarios. Instruments used to count particles also provide the number density of particles within specific size intervals e.g. 0.41–0.55 μm, based on calibration with polystyrene latex spheres and adjustments to account for the optical properties of particles [5, 62]. We selected the midpoint of the smallest three intervals: 0.48 μm, 0.63 μm, and 0.81 μm to represent the particles within those intervals, which contributed 51.9%, 24.7%, and 15.6% of the particle concentration, respectively. The remaining particles ranging from 0.92 μm to 2.98 μm were represented by a single particle size, 1.18 μm, which contributed 7.8% of the particle concentration. The simplified particle size distribution used here is broadly similar to the size distribution measured by another method [3, 4].

The 3D CFPD simulations were performed using second-order upwind schemes to improve the accuracy and the coupled pressure-velocity algorithm to handle the mass conservation relations. To ensure numerical stability for flow dynamics equilibrium at the temporal microscale, the fluid dynamic time step was 1×10^{-5} s. Once the flow was in equilibrium particles were injected through the filter inlet at particle time steps between $1 \times 10^{-4}-1 \times 10^{-3}$ s. Particle dynamics were tracked at each iteration. Convergence of the continuous phase was achieved when all residuals, as the approximated numerical error levels out in the continuous phase, became $<<$ 0.1%. In the case of the discrete phase analysis, the metric for error was based on the numerical ratios of the mass of injected aerosols per group size (i.e. 0.48 μm, 0.63 μm, 0.81 μm, and 1.18 μm), so that these ratios were consistent with the analytical aerosol mass ratio per liter of fluid volume and flowrate. The numerical ratio of aerosol mass per particle group size was approximately 1% or less of the analytical value in all flowrate cases studied.

5. Results

5.1. Fluid flow dynamics

Figure 3 compares the velocity magnitude normalized by the maximum velocity encountered in all cases, approximately $207\,m \cdot s^{-1}$ (at $1.2\,L \cdot s^{-1}$). The kinetic energy was also examined and normalized by the maximum value in all cases, which was approximately $1.12\,m^2 \cdot s^{-2}$ (at $1.2\,L \cdot s^{-1}$). The average normalized values of fluid flow velocity $\bar{u}_{avg}$ and fluid flow kinetic energy $\bar{E}_{avg}$ were obtained via area-weighted formulations. The volumes around the edges of the

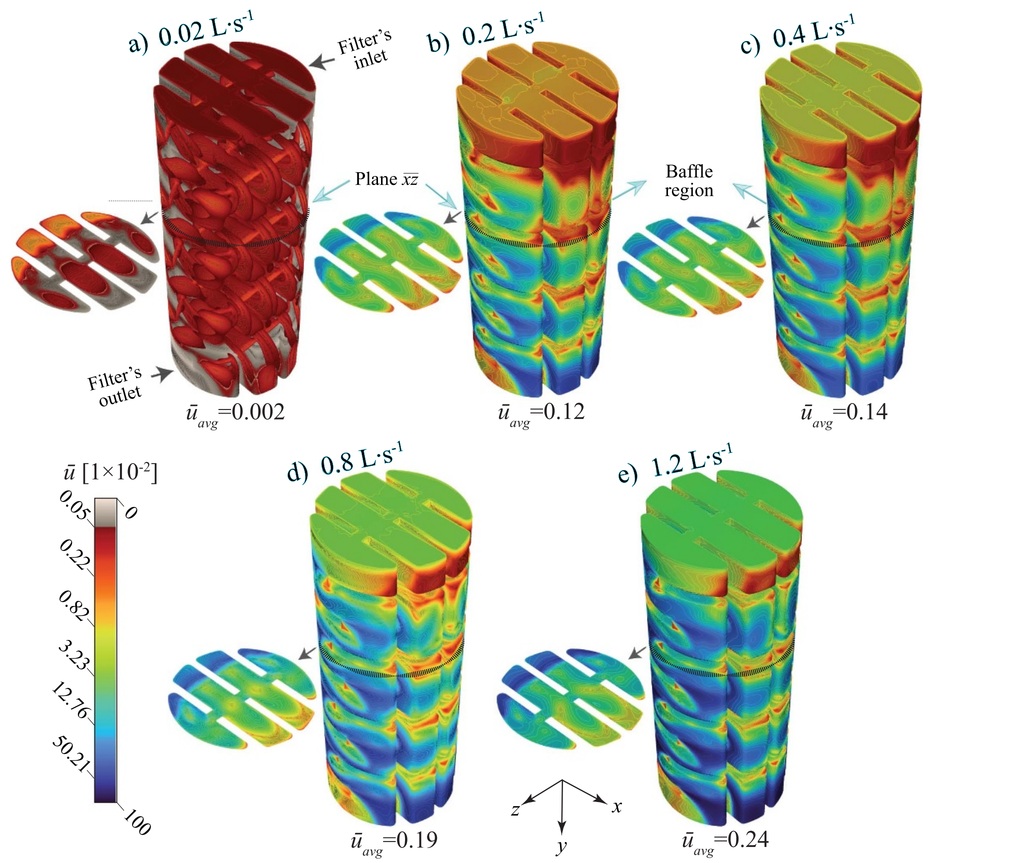

Figure 3. Fluid phase dynamics of simulated breath showing dimensionless velocity magnitude at: (a) $0.02\,\mathrm{L\cdot s^{-1}}$, (b) $0.2\,\mathrm{L\cdot s^{-1}}$, (c) $0.4\,\mathrm{L\cdot s^{-1}}$, (d) $0.8\,\mathrm{L\cdot s^{-1}}$, and (e) $1.2\,\mathrm{L\cdot s^{-1}}$. *The color legend is nonlinear to cover the two orders of magnitude velocity range. Cut* $\overline{xz}$ *plane is* $y = 8$ mm *from filter inlet's cross section.*

baffles in the filter promoted peaks of high velocity in the fluid flow, creating local high velocity gradients. At the lowest flowrate of $0.02\,\mathrm{L\cdot s^{-1}}$ and an initial Reynolds number (i.e. at the filter inlet), Re_i, of 207, $\bar{u}_{\mathrm{avg}} = 2\times10^{-3}$ and local values of Re of up to 2242 were registered relatively close to the baffle edges. A relatively linear response of $\bar{u}_{\mathrm{avg}}$ versus flowrate was found, with 0.12, 0.14, 0.19, and 0.24 at $0.2\,\mathrm{L\cdot s^{-1}}$, $0.4\,\mathrm{L\cdot s^{-1}}$, $0.8\,\mathrm{L\cdot s^{-1}}$, and $1.2\,\mathrm{L\cdot s^{-1}}$, respectively, resulting in Re_i 2047, 3960, 8186, and 12 232, respectively. Thus, under classical Re theory (i.e, a Newtonian fluid in motion in an infinitely long and smooth cylinder), the fluid velocity linearity remains in both flow regime conditions at the inlet of the filter: (a) the transition to turbulent regime ($2000 \leqslant \mathrm{Re}_i \leqslant 4000$) and (b) the turbulent regime ($\mathrm{Re}_i > 4000$). $\bar{E}_{\mathrm{avg}}$ was approximately 4×10^{-4} at $0.02\,\mathrm{L\cdot s^{-1}}$, which was a minimum of three orders of magnitude lower as compared to other flowrate cases (sublinear response), being: 0.28, 0.39, 0.66, and 1 corresponding to flowrates of $0.2\,\mathrm{L\cdot s^{-1}}$, $0.4\,\mathrm{L\cdot s^{-1}}$, $0.8\,\mathrm{L\cdot s^{-1}}$, and $1.2\,\mathrm{L\cdot s^{-1}}$, respectively. Similarly, the volume-average of turbulent intensity were: 27% (sublinear response), 1847%, 2242%, 3024%, and 3794% corresponding to flowrate cases of $0.02\,\mathrm{L\cdot s^{-1}}$, $0.2\,\mathrm{L\cdot s^{-1}}$, $0.4\,\mathrm{L\cdot s^{-1}}$, $0.8\,\mathrm{L\cdot s^{-1}}$, and $1.2\,\mathrm{L\cdot s^{-1}}$, respectively.

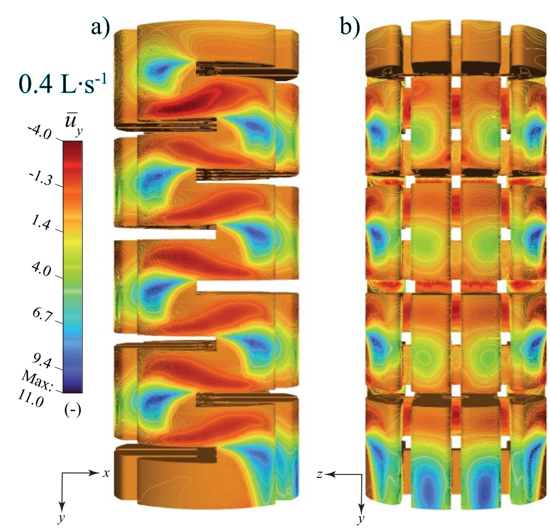

Figure 4. Normalized fluid stream velocity at $0.4\,\mathrm{L\cdot s^{-1}}$ in 2D views (a) *xy* and (b) *yz*.

Figure 4 illustrates the normalized fluid stream velocity $\bar{u}_y$ (along the y axis) developed inside the filter at $0.4\,\mathrm{L\cdot s^{-1}}$, which locally increased up to approximately 11-fold around baffle edges, denoted by blue regions. In contrast, figure 4 also shows that

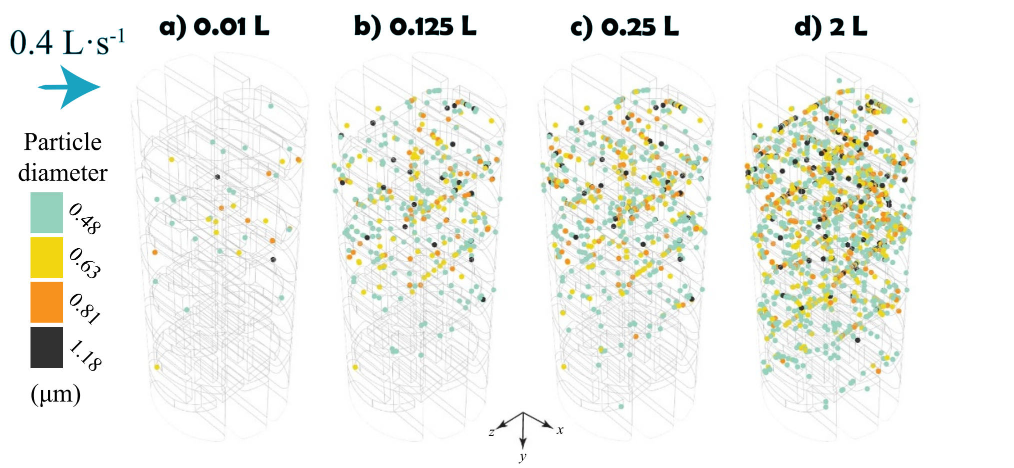

Figure 5. Distribution of particles deposited at $0.4\,\mathrm{L\cdot s^{-1}}$ after (a) 0.01 L, (b) 0.125 L, (c) 0.25 L, and (d) 2 L of fluid flow through the filter. Dots represent aerosol particles in the position where they deposited on the filter wall for each group of particle size as indicated by set of colors. *Model uncertainty ≈ 0.54% (see section 4). All particles are not shown and the particles shown are not to scale. Particle distributions may not accurately represent mass deposition due to particle overlapping in the 3D to 2D projections.*

there were regions of low to opposite (upstream) velocity, wherein some fluid flowlines were either stagnant in the filter or directed towards the inlet, denoted by red regions. These velocity accelerations and decelerations were found to be consistent in magnitude in all flowrate cases and as such were induced primarily by the abrupt geometric changes of the baffle arrangement and enhanced by turbulent eddies.

5.2. Aerosol dynamics: transport, distribution, and deposition

Under the conditions examined in this study, Brownian forces had negligible contribution to aerosol mass deposition or spatial distribution across all particle size groups. Thus, all aerosol particles in this study were considered deposited via impaction, interception, and/or turbulent dispersion.

Figure 5 depicts particle distribution after 0.01 L, 0.125 L, 0.25 L and 2 L of fluid flow through the filter at $0.4\,\mathrm{L\cdot s^{-1}}$. After 0.01 L of fluid volume, the simulation was not at equilibrium, showing an aerosol mass deposition of 72.8% *by mass*. For all other fluid volumes (0.125 L, 0.25 L and 2 L), equilibrium was attained, resulting in a consistent aerosol mass deposition of 93.6% *by mass*. The smallest particles, $0.48\,\mu$m in diameter, had a more uniform distribution throughout the filter than the larger particles. This was due to fluid forces driven by turbulent dispersion and interception deposition mechanisms. Approximately 8.6% of the aerosol mass of these smallest particles had no interaction with the wall and were thus lost in the fluid flowlines. The distribution of the larger particle sizes was less uniform in the filter, indicating an increase in the particle inertia and a corresponding increase in deposition by impaction.

Figure 6 depicts particle distribution corresponding to 0.25 L for all flowrates. Aerosol mass deposition in% *by mass* was 29.5, 85.6, 93.6, 98.5, and 99.9 at $0.02\,\mathrm{L\cdot s^{-1}}$, $0.2\,\mathrm{L\cdot s^{-1}}$, $0.4\,\mathrm{L\cdot s^{-1}}$, $0.8\,\mathrm{L\cdot s^{-1}}$, and $1.2\,\mathrm{L\cdot s^{-1}}$, respectively. As established in the particle distribution presented in figure 5, the aerosol mass deposition is independent (within uncertainty) of fluid volume once the simulation has reached equilibrium. At $0.02\,\mathrm{L\cdot s^{-1}}$, figure 6(a), low fluid velocities hindered deposition of even the largest particles ($1.18\,\mu$m diameter), and all deposited particles regardless of size were uniformly distributed. This revealed that the primary mechanism for aerosol deposition, which was only 29.5% *by mass*, was turbulent dispersion. The majority of aerosol mass was lost to the fluid exiting the filter outlet due to extremely low fluid flow velocities (as previously shown in figure 3(a). Thus, fluid flow forces dominated over particle inertial forces. Deposition by impaction did not likely occur due to low particle inertia as particles were subjected to eddy forces and the instantaneous fluid flowlines. The flowrate of $0.2\,\mathrm{L\cdot s^{-1}}$, figure 6(b), resulted in a relatively high mass deposition, suggesting inertial impaction was the main deposition mechanism. However, a fairly uniform spatial distribution of aerosols deposited on the filter wall was also indicative that a fraction of the aerosol cloud was still in-motion with the instantaneous flow velocity through the filter before being intercepted and/or collected via turbulent dispersion.

As flowrate increased and considering the abrupt velocity changes in both magnitude and direction driven by the geometry of the filter, particle inertial forces dramatically increased, which aided particles to deviate from the flow streamlines upon injection into the filter, keeping their original trajectory. Thus, deposition occurs by impaction, primarily enhanced by high fluid velocity and kinetic energy. As shown

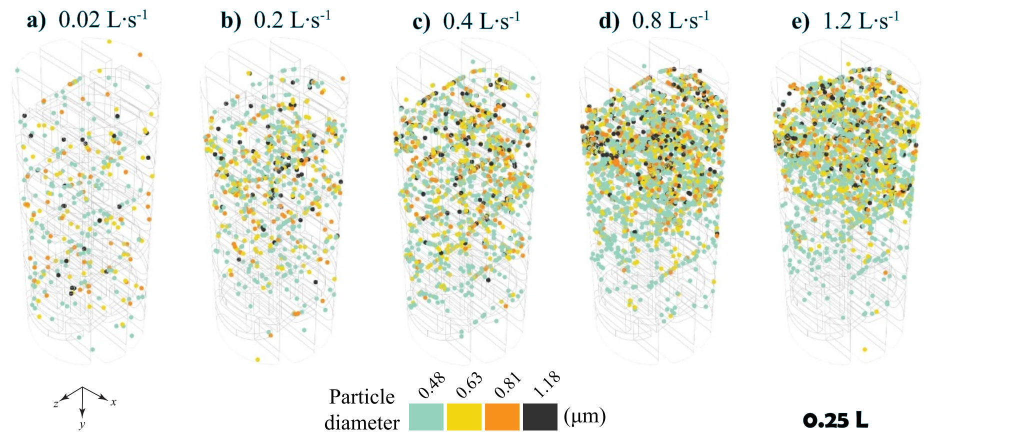

Figure 6. Distribution of particles deposited after 0.25 L of fluid flow through the filter at (a) $0.02\,\mathrm{L\cdot s^{-1}}$, (b) $0.2\,\mathrm{L\cdot s^{-1}}$, (c) $0.4\,\mathrm{L\cdot s^{-1}}$, (d) $0.8\,\mathrm{L\cdot s^{-1}}$, and (e) $1.2\,\mathrm{L\cdot s^{-1}}$. Dots represent aerosol particles in the position where they deposited on the filter wall for each group of particle size as indicated by set of colors. *Model uncertainty 0.13%–1.13% (see section 4). All particles are not shown and the particles shown are not to scale. Particle distributions may not accurately represent mass deposition due to particle overlapping in the 3D to 2D projections.*

in figures 6(c)–(e), aerosols impacted the filter wall shortly after injection and mainly deposited in the first half of the filter, particularly in the case of larger particles due to higher inertial forces, which was more accentuated at $0.8\,\mathrm{L\cdot s^{-1}}$ and $1.2\,\mathrm{L\cdot s^{-1}}$ with minimal aerosol loss. The results of particle spatial distribution and mass deposition indicate that particle inertia significantly dominates and controls the fluid-particulate dynamics at flowrates of $0.4\,\mathrm{L\cdot s^{-1}}$ and up. In these cases, turbulent dispersion was likely not contributing significantly to particle deposition as the high inertia of the aerosols reduced the effect of eddies on their original trajectory. Due to the high complexity of inertia and unsteady velocity of small particles in turbulent and multiphasic flows, an accurate analysis of turbulent dispersion, which is a complicated dispersion study [59], was beyond the scope of the present study.

Figure 7(a) presents the maximum Stokes number $\mathrm{St_a}$ and figure 7(b) presents aerosol deposition, both as a function of flowrate. In figure 7(a), the mean velocity was taken near the baffle edge regions of the filter and the shaded regions are an interpretation of aerosol deposition mechanisms investigated in this work. In figure 7(b), the dramatic effect of flowrate on aerosol deposition was quantified as a function of particle size. It was also apparent that the contribution of particle size to mass deposition is less significant in extreme (low or high) flowrate scenarios.

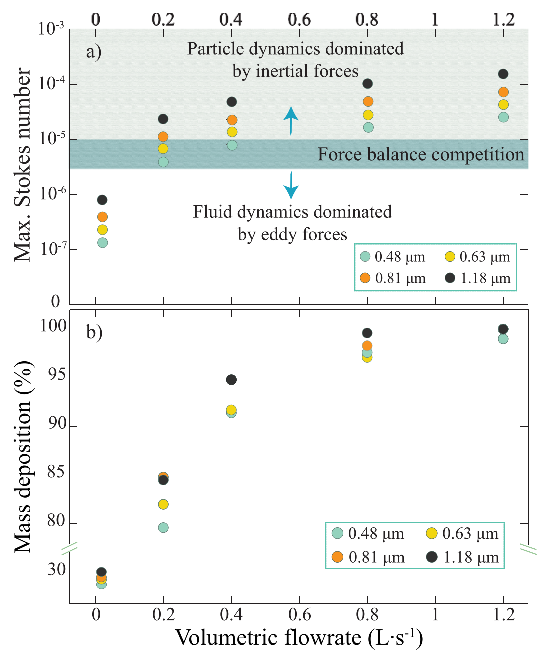

Figure 7. Aerosol deposition as a function of fluid flowrate per group of particle size: 0.48 μm, 0.63 μm, 0.81 μm, and 1.18 μm: (a) Interpretation of deposition mechanisms based on aerosol Stokes number at maximum fluid velocity (mean velocity value near baffle edges) and (b) Mass deposition. *Note: deposition is approximately equal in 0.48 μm, 0.63 μm and 0.81 μm particles at $0.4\,\mathrm{L\cdot s^{-1}}$; similarly, 0.63 μm, 0.81 μm, and 1.18 μm particles have approximately the same deposition at $1.2\,\mathrm{L\cdot s^{-1}}$.*

1. At $0.8\,\mathrm{L\cdot s^{-1}}$ and $1.2\,\mathrm{L\cdot s^{-1}}$, there was high mass deposition regardless of particle size. Because of high velocity gradients (figures 3(d) and (e)), particle inertial forces became dominant even in the smallest aerosols, as previously shown in figures 6(d) and (e). $\mathrm{St_a}$ was between 10^{-5} and 10^{-3} and the dominant mechanism is impaction. This indicates a deviation from classical Stokes number (see equation (8)) wherein particle inertial forces are only considered significant when $\mathrm{St_a} \gg 1$. Previous studies, both numerical and empirical, concentrated on respiratory tract characteristics have concluded that the inertial limit for submicrometer size particles has significant influence on aerosol deposition [67] at extremely low St_a, on the order of approximately 10^{-5} [68, 69] and even approximately 10^{-6} [69],

depending on the region of the respiratory tract. In contrast, interception of aerosols primarily by eddy forces was found to occur at $\mathrm{St_a}$ values lower than 10^{-5}.

2. At $0.2\,\mathrm{L\cdot s^{-1}}$ and $0.4\,\mathrm{L\cdot s^{-1}}$, particles were deposited by impaction or turbulent dispersion. When $\mathrm{St_a} \approx 10^{-5}$, the force balance competition between inertial forces and flow forces leads to more spread in mass deposition as a function of particle size.
3. At $0.02\,\mathrm{L\cdot s^{-1}}$, there was low mass deposition regardless of particle size. Because of low velocity gradients, particles were completely dominated by the flow field dynamics. $\mathrm{St_a} \leqslant 10^{-6}$ and the dominant mechanism is turbulent dispersion with a minor contribution of interception.

While the $\mathrm{St_a}$ metric provides a useful means to rationalize the observed results, in general, the question we must pose is how to predict whether a small exhaled breath aerosol will diverge from the fluid flow in an impaction filter. Numerical-empirical study feedback will aid in the development of more accurate multiscale particle transport models for quantitative analysis. These models, in addition to effectively resolving continuous contours of deposition, will closely capture the influence of finite particle inertia in filters of complex geometry involving multiphase dynamics. For the specific device under investigation here, numerical simulations of one impaction filter demonstrate that relatively high flowrates ensure high particle deposition efficiency above 95% *by mass*. In contrast, the flowrates corresponding to unguided human subjects result in a wide range of particle deposition efficiencies, approximately 30%–95% *by mass*. As many breath tests seek to understand the effect of an intervention, which includes drug use, sampling reproducibility can be improved by specifying an exhalation flowrate in addition to measures already employed such as breath volume or number of exhalations [25]. Even if the exhalation flowrate is not specified, measuring this flowrate with a spirometer may provide information to identify outliers within subjects or between subjects.

6. Conclusions

We developed a 3D CFPD model to simulate and visualize the trajectories and mass deposition of exhaled aerosols in an impaction filter of a commercial breath aerosol collection device. The Euler-Lagrangian modeling approach aided interpretation of exhaled fluid flow and particulate dynamics by decoupling the effects of human (exhaled flowrate) and filter (geometry) factors, as well as the contribution of various particle sizes in polydisperse aerosol clouds, which ranged between 0.48 μm and 1.18 μm in diameter. Aerosol mass deposition was primarily determined by the competition between particle forces and fluid forces, showing a higher aerosol mass deposition for increasing flowrates. High gradients of velocity in complex geometric features of the filter promoted significant aerosol mass deposition due to inertial forces that became largely dominant and thereby controlled the fluid-particle dynamics, aerosol deposition, and spatial distribution via impaction. The higher the inertial force, the less the influence of particle size on mass deposition, causing aerosols of all sizes to deposit immediately upon injection in the first half of the filter. The lowest flowrate we investigated resulted in significantly lower mass deposition of aerosols, approximately one fourth of the mass deposited at high flowrates and was uniformly distributed inside the filter primarily due to turbulent dispersion with some contribution of interception. Smaller aerosol particles were noticeably more susceptible to be deposited by interception and turbulent dispersion or lost through the outlet at the lower flowrates investigated. Particles deposited by impaction had Stokes number between 10^{-5} and 10^{-3}, whereas particles deposited by interception and turbulent dispersion had Stokes number of $\approx 10^{-6}$ and lower. Due to the complexity of the dynamics between exhaled fluid flow aerosol phenomena, results suggest further exhaled breath research needs to be carried out to re-evaluate breath volume as the primary metric currently used to predict aerosol mass deposition in breath aerosol collection devices.

Data availability statement

The data cannot be made publicly available upon publication because they contain commercially sensitive information. The data that support the findings of this study are available upon reasonable request from the authors.

Acknowledgments

This research was supported in part by funding from the National Institute of Justice, Office of Justice Programs, U.S. Department of Justice (DJO-NIJ-19-0008 and DJO-NIJ-22-0003, PIs: KMJ and TML). Munkplast AB, the manufacturer of the BreathExplor device, provided files of the device geometry. The funders and the manufacturer had no role in study design, data collection, analysis, decision to publish, or manuscript preparation. The opinions, findings, conclusions, or recommendations expressed in this publication are those of the authors and do not necessarily reflect those of NIST, NIJ, the Department of Commerce, or the Department of Justice.

ORCID iDs

Veruska Malavé https://orcid.org/0000-0002-5672-576X
Kavita Jeerage https://orcid.org/0000-0003-1210-6913
Edward Garboczi https://orcid.org/0000-0002-8973-1330
Tara Lovestead https://orcid.org/0000-0002-5614-5714

References

[1] Wang C, Prather K, Sznitman J, Jimenez J, Lakdawala S, Tufekci Z and Marr L 2021 Airborne transmission of respiratory viruses *Science* **373** eabd9149

[2] Almstrand A-C, Ljungström E, Lausmaa J, Bake B, Sjövall P and Olin A-C 2009 Airway monitoring by collection and mass spectrometric analysis of exhaled particles *Anal. Chem.* **81** 662–8

[3] Schwarz K, Biller H, Windt H, Koch W and Hohlfeld J 2010 Characterization of exhaled particles from the healthy human lung – a systematic analysis in relation to pulmonary function variables *J. Aerosol Med. Pulm. Drug Deliv.* **23** 371–9

[4] Schwarz K, Biller H, Windt H, Koch W and Hohlfeld J 2015 Characterization of exhaled particles from the human lungs in airway obstruction *J. Aerosol Med. Pulm. Drug Deliv.* **28** 52–58

[5] Almstrand A-C, Bake B, Ljungström E, Larsson P, Bredberg A, Mirgorodskaya E and Olin A-C 2010 Effect of airway opening on production of exhaled particles *J. Appl. Physiol.* **108** 584–8

[6] Holmgren H, Gerth E, Ljungström E, Larsson P, Almstrand A-C, Bake B and Olin A-C 2013 Effects of breath holding at low and high lung volumes on amount of exhaled particles *Respir. Physiol. Neurobiol.* **185** 228–34

[7] Veldhuizen E and Haagsman H 2000 Role of pulmonary surfactant components in surface film formation and dynamics *Biochim. Biophys. Acta* **1467** 255–70

[8] Larsson P, Mirgorodskaya E, Samuelsson L, Bake B, Almstrand A-C, Bredberg A and Olin A-C 2012 Surfactant protein a and albumin in particles in exhaled air *Respir. Med.* **106** 197–204

[9] Larsson P, Lärstad M, Bake B, Hammar O, Bredberg A, Almstrand A-C, Mirgorodskaya E and Olin A-C 2015 Exhaled particles as markers of small airway inflammation in subjects with asthma *Clin. Physiol. Funct. Imaging* **37** 489–97

[10] Tinglev A, Ullah S, Ljungkvist G, Viklund E, Olin A-C and Beck O 2016 Characterization of exhaled breath particles collected by an electret filter technique *J. Breath Res.* **10** 026001

[11] Larsson P, Bake B, Wallin A, Hammar O, Almstrand A-C, Lärstad M, Ljungström E, Mirgorodskaya E and Olin A-C 2017 The effect of exhalation flow on endogenous particle emission and phospholipid composition *Respir. Physiol. Neurobiol.* **243** 39–46

[12] Papineni R and Rosenthal F 1997 The size distribution of droplets in the exhaled breath of healthy human subjects *J. Aerosol Med.* **10** 105–16

[13] Bake B, Larsson P, Ljungkvist G, Ljungström E and Olin A-C 2019 Exhaled particles and small airways *Respir. Res.* **20** 8

[14] Wallace M, Pleil J and Madden M 2019 Identifying organic compounds in exhaled breath aerosol: non-invasive sampling from respirator surfaces and disposable hospital masks *J. Aerosol Sci.* **137** 105444

[15] Pleil J and Giese R 2017 Integrating exhaled breath diagnostics by disease-sniffing dogs with instrumental laboratory analysis *J. Breath Res.* **11** 032001

[16] Borras E, Cheng A, Wun T, Reese K, Frank M, Schivo M and Davis C 2019 Detecting opioid metabolites in exhaled breath condensate (EBC) *J. Breath Res.* **13** 046014

[17] Lovestead T and Bruno T 2017 Determination of cannabinoid vapor pressures to aid in vapor phase detection of intoxication *Forensic Chem.* **5** 79–85

[18] Skoglund C, Hermansson U and Beck O 2015 Clinical trial of a new technique for drugs of abuse testing: a new possible sampling technique *J. Subst. Abuse Treat.* **48** 132–6

[19] Beck O, Ullah S and Kronstrand R 2019 First evaluation of the possibility of testing for drugged driving using exhaled breath sampling *Traffic Inj. Prev.* **20** 238–43

[20] Olla P, Ishraque M and Bartol S 2020 Evaluation of breath and plasma tetrahydrocannabinol concentration trends postcannabis exposure in medical cannabis patients *Cannabis Cannabinoid Res.* **5** 99–104

[21] Himes S, Scheidweiler K, Beck O, Gorelick D, Desrosiers N and Huestis M 2013 Cannabinoids in exhaled breath following controlled administration of smoked cannabis *Clin. Chem.* **59** 1780–9

[22] Wurz G and DeGregorio M 2022 Indeterminacy of cannabis impairment and Δ^9-tetrahydrocannabinol (Δ^9–THC) levels in blood and breath *Sci. Rep.* **12** 8323

[23] Seferaj S, Ullah S, Tinglev A, Carlsson S, Winberg J, Stambeck P and Beck O 2018 Evaluation of a new simple collection device for sampling of microparticles in exhaled breath *J. Breath Res.* **12** 036005

[24] Feltmann K, Elgán T, Böttcher M, Lierheimer S, Hermansson S, Beck O and Gripenberg J 2022 Feasibility of using breath sampling of non-volatiles to estimate the prevalence of illicit drug use among nightlife attendees *Sci. Rep.* **12** 20283

[25] Jeerage K, Beuning C, Friss A, Bidwell C and Lovestead T 2023 THC in breath aerosols collected with an impaction filter device before and after legal-market product inhalation–a pilot study *J. Breath Res.* **17** 037103

[26] Mingxiao L, Biswas S, Nantz M, Higashi R and Fu X-A 2013 A microfabricated preconcentration device for breath analysis *Sensors Actuators* B **180** 130–6

[27] Kalidoss R, Umapathy S and Rani Thirunavukkarasu U 2021 A breathalyzer for the assessment of chronic kidney disease patients' breathprint: breath flow dynamic simulation on the measurement chamber and experimental investigation *Biomed. Signal Process. Control* **70** 103060

[28] Haslbeck K, Schwarz K, Hohlfeld J, Seume J and Koch W 2010 Submicron droplet formation in the human lung *J. Aerosol Sci.* **41** 429–38

[29] Tu J, Inthavong K and Ahmadi G 2013 *Computational Fluid and Particulate Dynamics in the Human Respiratory System* (Springer)

[30] Koullapis P, Stylianou F, Lin C-L, Kassinos S and Sznitman J 2021 In *silico* methods to model dose deposition *Inhaled Medicines, Optimizing Development Through Integration of In Silico, In Vitro and In Vivo Approaches* ed S Kassinos, P Bckman, J Conway and A Hickey (Springer)

[31] Bui V, Moon J-Y, Chae M, Park D and Lee Y-C 2020 Prediction of aerosol deposition in the human respiratory tract via computational models: a review with recent updates *Atmosphere* **11** 137

[32] Longest P, Bass K, Dutta R, Rani V, Thomas M, El-Achwah A and Hindle M 2019 Use of computational fluid dynamics deposition modeling in respiratory drug delivery *Expert Opin. Drug Deliv.* **16** 7–26

[33] Longest P, Vinchurkar S and Martonen T 2006 Role of CFD based in silico modelling in establishing an in vitro–in vivo correlation of aerosol deposition in the respiratory tract *J. Aerosol Sci.* **37** 1234–57

[34] Kolanjiyil A, Hosseini S, Alfaifi A, Farkas D, Walenga R, Babiskin A, Hindle M, Golshahi L and Longest P 2022 Validating CFD predictions of nasal spray deposition: inclusion of cloud motion effects for two spray pump designs *Aerosol Sci. Technol.* **56** 305–22

[35] Huang F, Zhu Q, Zhou X, Gou D, Yu J, Li R, Tong Z and Yang R 2017 Role of CFD based in silico modelling in establishing an in vitro-in vivo correlation of aerosol deposition in the respiratory tract *Adv. Drug Deliv. Rev.* **170** 369–85
[36] Xi J and Longest P 2007 Transport and deposition of micro–aerosols in realistic and simplified models of the oral airway *Ann. Biomed. Eng.* **35** 560–81
[37] Xi J, Kim J, Si X, Corley R, Kabilan S and Wang S 2015 CFD modeling and image analysis of exhaled aerosols due to a growing bronchial tumor: towards non-invasive diagnosis and treatment of respiratory obstructive diseases *Theranostics* **5** 443–55
[38] Hossain M and Faisal N 2021 Modeling aerosol cloud aerodynamics during human coughing, talking and breathing actions *AIP Adv.* **11** 045111
[39] Dbouk T and Drikakis D 2020 On respiratory droplets and face masks *Phys. Fluids* **32** 063303
[40] Haghnegahdar A, Zhao J and Feng Y 2019 Lung aerosol dynamics of airborne influenza a virus-laden droplets and the resultant immune system responses: an in silico study *J. Aerosol Sci.* **134** 34–55
[41] Pendar M-R and Páscoa J 2020 Numerical modeling of the distribution of virus carrying saliva droplets during sneeze and cough *Phys. Fluids* **32** 083305
[42] Fabregat F, Vernet A, Dutta S, Mittal K and Pallarès J 2021 Direct numerical simulation of the turbulent flow generated during a violent expiratory event *Phys. Fluids* **33** 035122
[43] Sheikhnejad Y, Aghamolaei R, Fallahpour M, Motamedi H, Moshfeghi M, Mirzaei P and Bordbar H 2022 Airborne and aerosol pathogen transmission modeling of respiratory events in buildings: an overview of computational fluid dynamics *Sustain. Cities Soc.* **79** 103704
[44] Feng Y, Zhao J, Spinolo M, Lane K, Leung D, Marshall D and Mlinaric P 2021 Assessing the filtration effectiveness of a portable ultraviolet air cleaner on airborne SARS-CoV-2 laden droplets in a patient room: a numerical study *Aerosol Air Qual. Res.* **21** 20608
[45] Löhner R, Antil H and Idelsohn S 2020 Detailed simulation of viral propagation in the built environment *Comput. Mech.* **66** 1093–107
[46] Mirzaie M, Lakzian E, Khan A, Warkiani M, Mahian O and Ahmadi G 2021 COVID-19 spread in a classroom equipped with partition: a CFD approach *J. Hazard Mater.* **420** 126587
[47] Wilson J, Miller S and Mukherjee D 2021 A Lagrangian approach towards quantitative analysis of flow-mediated infection transmission in indoor spaces with application to SARS-COV-2 *Int. J. Comput. Fluid Dyn.* **35** 727–42
[48] Li Y-Y, Wand J-X and Chen X 2020 Can a toilet promote virus transmission? from a fluid dynamics perspective *Phys. Fluids* **32** 065107
[49] Mortazavi H, Beni H M, Islam M S and Paul G 2023 Aerosolized airborne bacteria and viruses inhalation: micro–bioaerosols deposition effects through upper nasal airway inhalation *Digital Human Modeling and Medicine* ed G Paul and M H Doweidar (Academic)
[50] Zhang W, Xiang Y, Lu C, Ou C and Deng Q 2020 Numerical modeling of particle deposition in the conducting airways of asthmatic children *Med. Eng. Phys.* **76** 40–46
[51] Atzeni C, Lesma G, Dubini G, Masi M, Rossi F and Bianchi E 2021 Computational fluid dynamic models as tools to predict aerosol distribution in tracheobronchial airways *Sci. Rep.* **11** 1109
[52] Schmidt A, Borras E, Kenyon N and Davis C 2020 Investigating the relationship between breath aerosol size and exhaled breath condensate (EBC) metabolomic content *J. Breath Res.* **14** 047104
[53] Zamuruyev K *et al* 2017 Human breath metabolomics using an optimized non-invasive exhaled breath condensate sampler *J. Breath Res.* **11** 016001
[54] Bass K, Farkas D, Hassan A, Bonasera S, Hindle M and Longest P 2021 High–efficiency dry powder aerosol delivery to children: review and application of new technologies *J. Aerosol Sci.* **153** 105692
[55] Xu C, Nielsen P, Gong G, Jensen R and Liu L 2015 Influence of air stability and metabolic rate on exhaled flow *Indoor Air* **25** 198–209
[56] ANSYS, Inc *ANSYS Commercial License, Release 2022 R2, Help System, Analysis Guide*
[57] Morsi A and Alexander S 1972 An investigation of particle trajectories in two-phase flow system *J. Fluid Mech.* **55** 193–208
[58] Jin C, Potts I and Reeks M 2015 A simple stochastic quadrant model for the transport and deposition of particles in turbulent boundary layers *Phys. Fluids* **31** 053305
[59] Crowe C, Schwarzkopf J and Tsuji M S Y 2012 *Multiphase Flows With Droplets and Particles* 2nd edn (CRC Press)
[60] Shih T-H, Liou W, Shabbir A, Yang Z and Zhu J 1995 A new $k-\varepsilon$ eddy viscosity model for high Reynolds number turbulent flows *Comput. Fluids* **24** 227–38
[61] Ma B and Lutchen K 2009 CFD simulation of aerosol deposition in an anatomically based human large –medium airway model *Ann. Biomed Eng.* **37** 271–85
[62] Holmgren H, Ljungström E, Almstrand A-C, Bake B and Olin A-C 2010 Size distribution of exhaled particles in the range from 0.01 to 2.0 μm *J. Aerosol Sci.* **41** 439–46
[63] Society A T and Society E R 2005 ATS/ERS recommendations for standardized procedures for the online and offline measurement of exhaled lower respiratory nitric oxide and nasal nitric oxide *Am. J. Respir. Crit. Care Med.* **171** 912–30
[64] Hankinson J, Odencrantz J and Fedan K 1999 Spirometric reference values from a sample of the general U.S. population *Am. J. Respir. Crit. Care Med.* **159** 179–87
[65] 2005 Behavior of aerosol particles *Inhaled Particles* (*Interface Science and Technology* vol 5), ed C-S Wang (Elsevier) ch 4, pp 55–78
[66] Johnson G and Morawska L 2009 The mechanism of breath aerosol formation *J. Aerosol Med. Pulmon. Drug Deliv.* **22** 229–37
[67] Arsalanloo A, Abbasalizadeh M, Khalilian M, Saniee Y, Ramezanpour A and Islam M 2022 A computational approach to understand the breathing dynamics and pharmaceutical aerosol transport in a realistic airways *Adv. Powder Technol.* **33** 103635
[68] Cohen B and Asgharian B 1990 Deposition of ultrafine particles in the upper airways: an empirical analysis *J. Aerosol Sci.* **21** 789–97
[69] Longest P and Xi J 2007 Computational investigation of particle inertia effects on submicron aerosol deposition in the respiratory tract *Aerosol Sci.* **38** 111–30